Science Advances
AAAS

Supplementary Materials for

Tailoring sub-3.3 Å ultramicropores in advanced carbon molecular sieve membranes for blue hydrogen production

Leiqing Hu, Vinh T. Bui, Ajay Krishnamurthy, Shouhong Fan, Wenji Guo, Sankhajit Pal, Xiaoyi Chen, Gengyi Zhang, Yifu Ding, Rajinder P. Singh, Monica Lupion, Haiqing Lin*

*Corresponding author. Email: haiqingl@buffalo.edu

Published 9 March 2022, *Sci. Adv.* **8**, eabl8160 (2022)
DOI: 10.1126/sciadv.abl8160

This PDF file includes:

Supplementary Text

Materials

Celazole® PBI S10 solution containing ≈ 9.5 wt% PBI (with a molecular weight of 35,000 Da) was purchased from PBI Performance Products Inc. (Charlotte, NC). PPA and methanol were obtained from Sigma-Aldrich Corporation (St. Louis, MO). Ultrapure H_2, CO_2, C_2H_6, and N_2 were provided by Airgas Inc. (Buffalo, NY).

Superior H_2/CO_2 Separation Performance of PBI-$PPA_{0.30}$/CMS600

Table S1 compares PBI-$PPA_{0.34}$ and PBI-$PPA_{0.30}$/CMS600 with cross-linked PBIs and leading CMS membrane materials for H_2/CO_2 separation. Among all cross-linked PBIs, PBI-$PPA_{0.34}$ shows the best combination of high H_2 permeability and high H_2/CO_2 selectivity at 150 °C (*21, 24, 25*). After the carbonization, the obtained PBI-$PPA_{0.30}$/CMS600 also displays H_2/CO_2 separation performance superior to other CMS materials (*4, 38-40, 44*). Fig. S1 also compares PBI-$PPA_{0.30}$/CMS600 with the leading inorganic membranes for H_2/CO_2 separation. The PBI-$PPA_{0.30}$/CMS600 shows one of the best H_2/CO_2 separation properties, in addition to the simplicity for the fabrication of the polymeric membranes compared with those inorganic membranes.

Determination of the PPA doping level

Fig. S2a presents the doping level of PBI-PPA films as a function of the molar ratio of PPA to the PBI repeating unit in the solutions. Increasing the acid amount in the solutions increases the doping level. At the same molar ratio, the thick films show a slightly lower doping level than the thin films due to the self-limiting diffusion, i.e., the gradual formation of cross-linking on the surface may limit PPA diffusion into the films. Fig. S2b displays the effect of the doping time on the doping level of PPA in a PBI thin film of ≈ 12 μm and a thick film of 50-70 μm. The doping level increases with increasing doping time and levels off after about 48 h for the thin film and about 120 h for the thick film. Therefore, the doping time in this study was set at nominally 72 h for the thin films and 168 h for the thick films to ensure that the acid is evenly distributed in the films.

Fourier-transform infrared (FTIR) spectra of PBI-PPA, PBI/CMS600, and PBI-$PPA_{0.30}$/CMS600

Fig. S3a illustrates the strong interaction between PPA and PBI by FTIR spectra of PBI-PPA films. The characteristic peak at 910 cm^{-1} representing the P−O bonding indicates the existence of PPA. The peaks at 870 and 945 cm^{-1} can be ascribed to $P(OH)_2$, which are somewhat diminished in intensity in the spectra of PBI-PPA, indicating the loss of protons in PPA due to proton transfer. Fig. S5a compares FTIR spectra of PBI, PBI-$PPA_{0.30}$, and their CMS films carbonized at 600 °C. The peaks at 3342, 1625, and 1290 cm^{-1} in the PBI represent −NH, C=N, and C−N bonds in the imidazole ring, respectively (*53*). The peak at 3342 cm^{-1} disappears in the spectrum of PBI-$PPA_{0.30}$ because of the hydrogen bonding between −NH and PPA. Those functional groups disappeared after carbonization, indicating the opening and degradation of imidazole rings.

Density of the PBI-PPA thin films

The density (ρ_b) of the PBI-PPA thin films can be described using an additive model:

$$\frac{1}{\rho_m} = \frac{\omega_p}{\rho_p} + \frac{\omega_a}{\rho_a} = \frac{1}{\rho_p} + \left(\frac{1}{\rho_a} - \frac{1}{\rho_p}\right)\omega_a \qquad \text{(Eq. S1)}$$

where ω is the weight fraction, and the subscripts of p and a represent the PBI and PPA, respectively. In this model, the density of PBI and PPA is assumed to be independent of their composition. As shown in Fig. S3b, the ρ_b can be satisfactorily modeled with a ρ_a valued of ≈ 2.25 g/cm^3 that is higher than the density (≈ 2.00 g/cm^3) of pure PPA, suggesting the tightened structure in the PBI. The results suggest that the PBI may have a different density from the pure PBI. However, there is no other way to obtain the density of PPA and PBI in PBI-PPA$_x$, which are needed for the analysis of the free volume. Therefore, the model is used in this study (*23*).

FFV of the PBI-PPA thin films

The specific volume of PBI-PPA films at around 150 ℃ can be estimated using Eq. S2 (*24*):

$$V_{150^\circ C} = V_{RT}\left(1+\overline{\alpha}_V \Delta T\right) \quad \text{(Eq. S2)}$$

where $V_{150^\circ C}$ and V_{RT} are the specific volume at 150 ℃ and 23 ℃, respectively. ΔT equals 127 K (i.e., the difference between 150 ℃ and 23 ℃). $\bar{\alpha}_V$ is the average volumetric thermal expansion coefficient in the PBI-PPA and can be estimated as (*24*):

$$\overline{\alpha}_V = \varphi_a \alpha_a + \varphi_p \alpha_p \quad \text{(Eq. S3)}$$

where φ_a and φ_p are volume fractions of the PPA and PBI respectively. α_a and α_p are volumetric thermal expansion coefficients of the PPA and PBI, respectively. The α_p is 6.9×10^{-5} K^{-1} (*24*). However, no α_a value was reported for PPA, and the value of 4.8×10^{-4} K^{-1} (α_a of phosphoric acid) was used due to their similar structures. The details of the calculation for the *FFV* at 150 ℃ are recorded in Table S3.

Gas transport properties of PBI-PPA thin films describing by the free volume model

The PPA doping mainly affects H_2 diffusivity (instead of solubility), and its permeability can be described using the free volume model:

$$P_A = A_P exp(-B_p / FFV) \quad \text{…….(Eq. S4)}$$

where A_p is a pre-exponential factor, and B_p is a constant related to the penetrant molecular size. Fig. S3c shows that both H_2 and CO_2 permeability can be described using the model with the B_p value of 0.28 for H_2 and 1.5 for CO_2, consistent with the larger molecular size of CO_2. Besides, H_2/CO_2 selectivity can also be satisfactorily described using the model.

TGA and DTA curves of PPA, PBI and PBI-PPA$_{0.34}$ thin films

Fig. S4 shows the TGA and DTA curves of PPA, PBI, and PBI-PPA$_{0.34}$, respectively. PPA starts to degrade at around 150 ℃ and displays two sharp DTA peaks at ≈ 300 ℃ (formation of $(HPO_3)_n$) and ≈ 600 ℃ (formation of P and P_2O_5). Besides, both PBI and PBI-PPA$_{0.34}$ films are thermally stable up to ≈ 200℃, and PBI-PPA$_{0.34}$ shows a mass loss between 200 and 400 ℃ due to the PPA decomposition. The introduction of the PPA decreases the decomposition temperature of PBI from ≈ 600 ℃ to ≈ 530 ℃. PBI and PBI-PPA$_{0.34}$ have a similar mass loss at 600 ℃, suggesting that the degraded PPA still exists in PBI at 600 ℃. Fig. S5b shows that the mass loss of PBI-PPA/CMS600 increases with increasing doping level due to the decomposition of PPA. Fig. S5c displays the Raman spectra, confirming the carbon structures.

Positron Annihilation Lifetime Spectroscopy (PALS) of PBI-PPA and their CMS films

Typical lifetimes (τ, ns) and their relative contributions or intensities (I, %) in polymers can be categorized as follows. The shortest lifetime is attributed to self-annihilation of para positronium (p-Ps), ($\tau_{p\text{-}Ps}$ or τ_1) at nominally 0.125 ns, the intermediate component is due to the direct

positron-electron annihilation lifetime (τ_2) at around 0.35 – 0.5 ns, and the longest is due to ortho-positronium "pick-off" lifetime ($\tau_{o\text{-}Ps}$ or τ_3) at around 1 – 5 ns. However, in the presence of functional groups having large electron affinity (such as the nitroaromatics consisting of imide functionalities used in the current study), there is often positron inhibition or quenching that can affect both the measured lifetimes and their relative intensities. Here, the lifetime analysis is conducted at intervals of 1 million counts until the maximum number of counts (nominally 4 million to 5 million counts in each case) to understand the possible effect of positron and positronium quenching over the data acquisition period. Specimens in this study predominantly exhibit at least one lifetime, $\tau_2 \approx 0.35 – 0.37$ ns that corresponds to positron-electron annihilation process and an additional $\tau_3 \approx 1 – 2$ ns component with low relative contributions. In scenarios where there is a τ_3, a nominal τ_1 contribution is expected, and this was accounted for by adding and constraining $\tau_1 \approx 125$ ps and assuming that the ratio of the $I_3/I_1 = 3$. The final analysis is derived based on the assumption that the samples contain a log-normal distribution of τ_2 (where the average τ_2 and its corresponding σ_2 are estimated) along with τ_1 and τ_3 (where positronium contributions are observed).

The semi-empirical Tao-Eldrup model is typically fit to τ_3 data to obtain an average radius of nanoscale pores (R) according to Eq. S4 when the contributions in $I_3 > 2$ %. The modified version of this equation (Eq. S5) can be utilized toward fitting τ_2 in samples that do not contain o-Ps contributions or when $I_3 < 2$ %. However, since the majority of the specimens in this study display positron/positronium quenching over the data acquisition period, only the lifetimes and their relative contributions from the first million counts is instead presented in Fig. S5d and Table S4.

$$\tau_3 = 0.5\left[1 - \frac{R}{R+1.656} + \frac{1}{2\pi}\sin\left(\frac{2\pi R}{R+1.656}\right)\right]^{-1} \quad \text{(Eq. S5)}$$

$$\tau_2 = 0.26\left[1 - \frac{R}{R+3.828} + \frac{1}{2\pi}\sin\left(\frac{2\pi R}{R+3.828}\right)\right]^{-1} \quad \text{(Eq. S6)}$$

Elemental analysis by EDS

Table S6 shows the elemental composition of the cross-section of the PBI-PPA$_{0.30}$ and PBI-PPA$_{0.30}$/CMS600 films. The measured P/C molar ratio in the PBI-PPA$_{0.34}$ and PBI-PPA$_{0.30}$ film are ≈ 0.034 and ≈ 0.028, respectively, which are close to their corresponding theoretical values (0.034 and 0.030, respectively). Both PBI-PPA$_{0.30}$ thick and PBI-PPA$_{0.30}$/CMS600 films show consistent N/C molar ratios and decreasing P/C molar ratios from the surface to the center, indicating that the PPA content is higher on the surface than the center caused by the self-limiting diffusion. The pyrolysis decreases the N/C ratio while retaining the P/C ratio, suggesting that the loss of the N but not for P after the pyrolysis.

Mechanical properties of PBI, PBI-PPA$_{0.30}$, and their derived CMS films

Fig. S5e,f shows strain-stress tensile plots of PBI, PBI-PPA$_{0.30}$, PBI/CMS500, and PBI/CMS550 obtained using the tensile test at 150 °C. The PPA doping decreases the fracture strain but increases the modulus value (Table S7), indicating that the acid doping leads to a ductile-to-brittle transition. PBI/CMS displays much lower fracture strains than PBI, and the strain decreases with the increasing carbonization temperature. It confirms that high carbonization temperature produces less flexible CMS membranes.

PBI/CMS600 and PBI-PPA$_{0.30}$/CMS films were too fragile to be tested using the tensile. Therefore, their mechanical properties were tested using the three-point flexural test, as shown in Fig. S5g,h. Both PBI/CMS500 and PBI-PPA$_{0.30}$/CMS500 have good extensibility and flexibility.

However, PBI/CMS600 and PBI-PPA$_{0.30}$/CMS600 display low strains and high modulus values (Table S7), indicating that the films are becoming stiff and rigid after the carbonization at 600 °C.

Table S8 records the mechanical properties of PBI or carbonized materials for H_2/CO_2 separation. Our PBI and CMS materials show comparable modulus and fracture strain compared with thermally rearranged (TR) polymers or other CMS materials.

Gas permeability of PBI-PPA thin films and PBI-PPA/CMS films

Fig. S6a,b shows that CO_2 permeability of PBI, PBI-PPA$_{0.34}$, PBI/CMS600, and PBI-PPA$_{0.30}$/CMS600 can be satisfactorily described using the Arrhenius equation with the parameters recorded in Table S9. The PPA doping increases the $E_{P,A}$ values for both H_2 and CO_2 because of the decreased *FFV*, and the carbonization decreases the $E_{P,A}$ value due to the increased *FFV*.

CO_2 diffusivity and its dependence on the temperature

Fig. S6c shows that CO_2 diffusivity can be satisfactorily described using the Arrhenius equation:

$$D_A = D_{0,A} exp(-E_{D,A}/RT) \quad \text{(Eq. S7)}$$

where $D_{0,A}$ is a pre-exponential factor, and $E_{D,A}$ is activation energy of the gas diffusion. The fitted values of $D_{0,A}$ and $E_{D,A}$ are recorded in Table S10. PBI-PPA$_{0.34}$ has higher $E_{D,A}$ value (42 kJ/mol) than PBI (39 kJ/mol), consistent with the lower free volume of PBI-PPA$_{0.34}$. After carbonization, $E_{D,A}$ value decreases due to the increased porosity. Interestingly, PBI-PPA$_{0.30}$/CMS600 has higher $E_{D,A}$ value (27 kJ/mol) than PBI/CMS600 (22 kJ/mol) because of the stronger size-sieving ability of PPA$_{0.30}$/CMS600.

Effects of T_C on physical properties of PBI/CMS

Fig. S7a shows that the bulk density, skeletal density, and porosity of PBI/CMS increase with increasing T_C due to the increased mass loss. By contrast, increasing the T_C value decreases the *d*-spacings for the CMS samples because of the densification, as shown in Fig. S7b. These results indicate that increasing T_C increases the concentration of the free volume elements but decreases their volume. All of the CMS samples exhibit higher *d*-spacing than their corresponding polymer precursors. Fig. S7c shows that the mass loss of both PBI/CMS and PBI-PPA$_{0.30}$/CMS increases with increasing T_C values.

Gas sorption isotherms of CMS samples

Fig. S8a,b displays CO_2 and C_2H_6 sorption isotherms of PBI/CMS600, PBI-PPA$_{0.30}$/CMS500, PBI-PPA$_{0.30}$/CMS550, and PBI-PPA$_{0.30}$/CMS600 at 150 °C, respectively. The sorption can be described using the dual-mode sorption model with the values of the adjustable parameters recorded in Table S5. C_H' values for CO_2 and C_2H_6 increase tremendously from PBI to PBI/CMS600 because of the increased porosity. By contrast, the carbonization of PBI-PPA$_{0.30}$ increases the C_H' value for CO_2, but decreases the C_H' value for C_2H_6, presumably because the newly created pores are too small for C_2H_6 to access. In general, increasing T_C values increases the C_H' values. Fig. 8c shows the effect of carbonization on the C_2H_6 solubility and CO_2/C_2H_6 solubility selectivity of PBI-PPA$_{0.30}$/CMS at 150 °C.

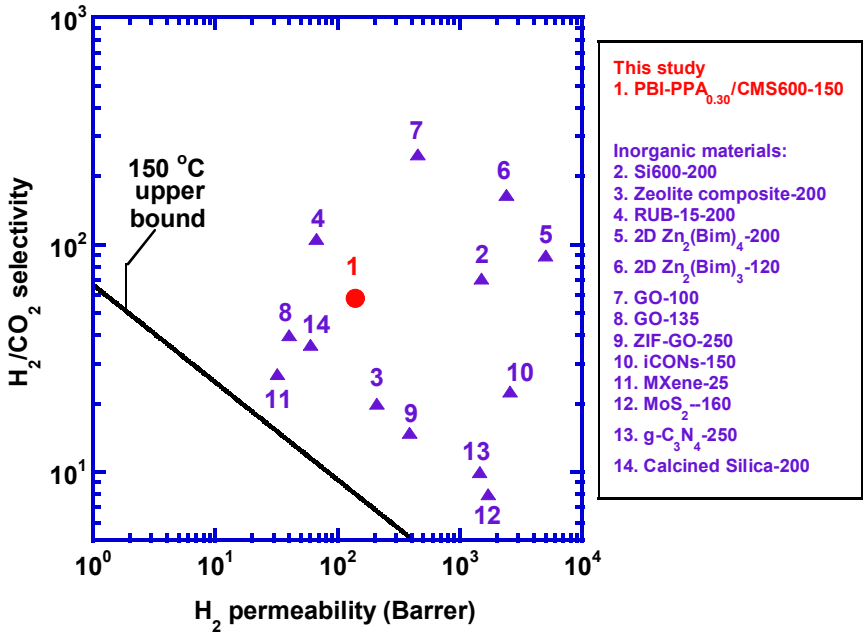

Fig. S1.
Superior H_2/CO_2 separation in PBI-PPA$_{0.30}$/CMS600, demonstrated by the comparison with the leading inorganic membranes for H_2/CO_2 separation. Details of these inorganic membranes are listed in Table S2.

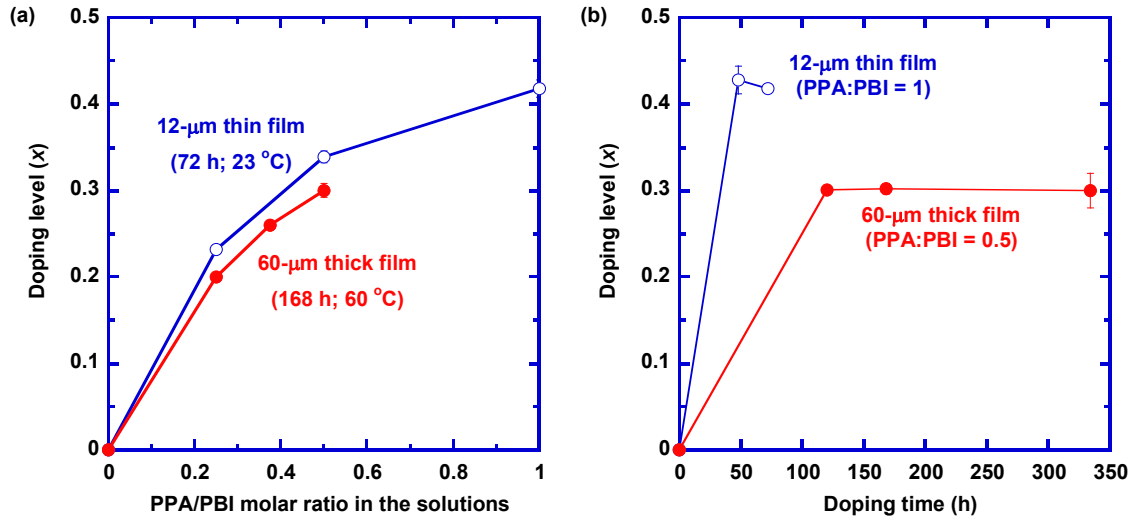

Fig. S2.
Manipulation of the PPA doping degree in PBI thin films. (a) Effect of the PPA/PBI molar ratio in the doping solutions on the doping level in the films at equilibrium. (b) Effect of the doping time on the doping level in PBI-PPA. The molar ratio of PPA to the PBI repeating unit in the solution is 1 for PBI thin films and 0.5 for thick films.

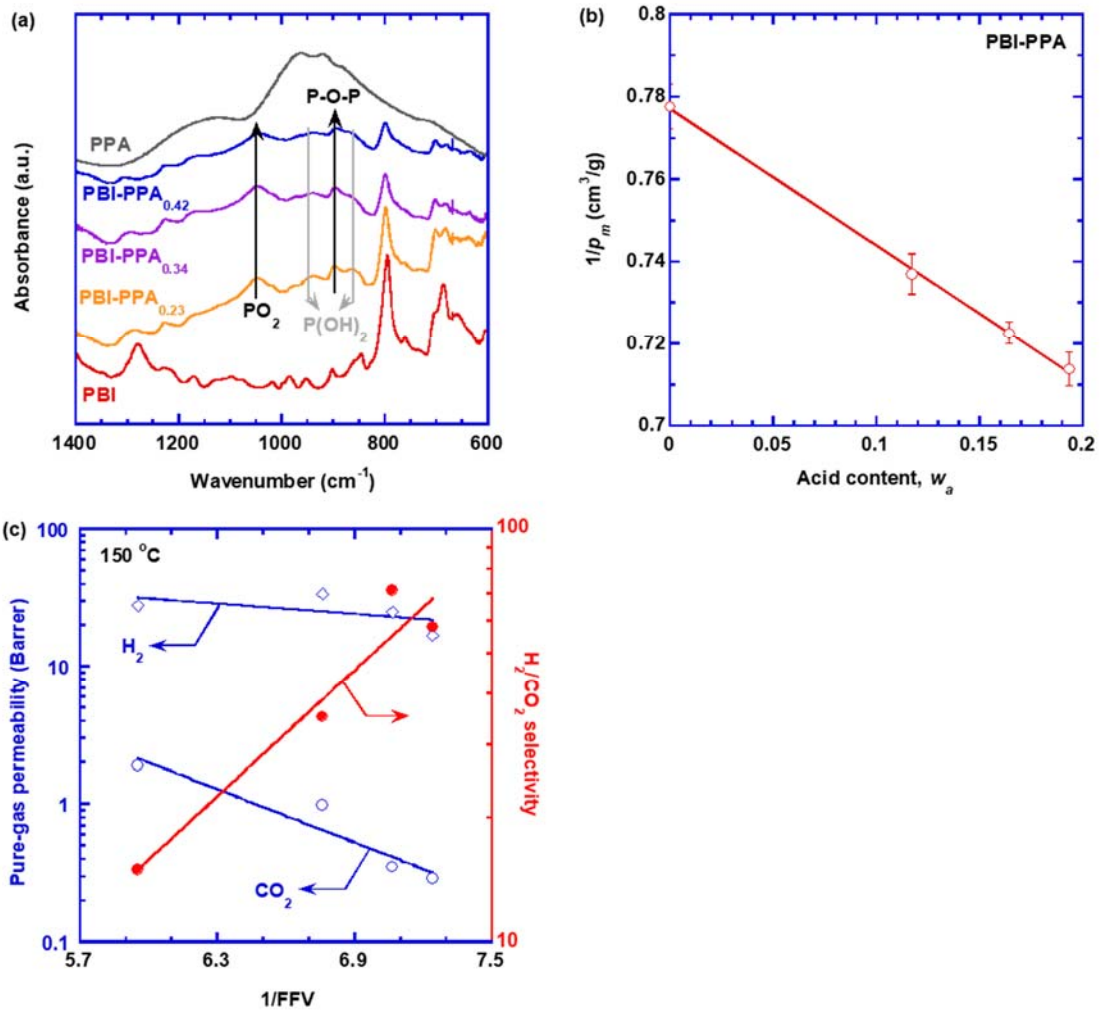

Fig. S3.
Physical and gas transport properties of PBI-PPA films. (a) FTIR spectra of PBI-PPA. (b) Correlation of $1/\rho_b$ with the ω_a in PBI–PPA using the additive model (Eq. S1). (c) Pure-gas H_2/CO_2 separation properties of PBI-PPA as a function of $1/FFV$. The lines are the best fits of Eq. (3).

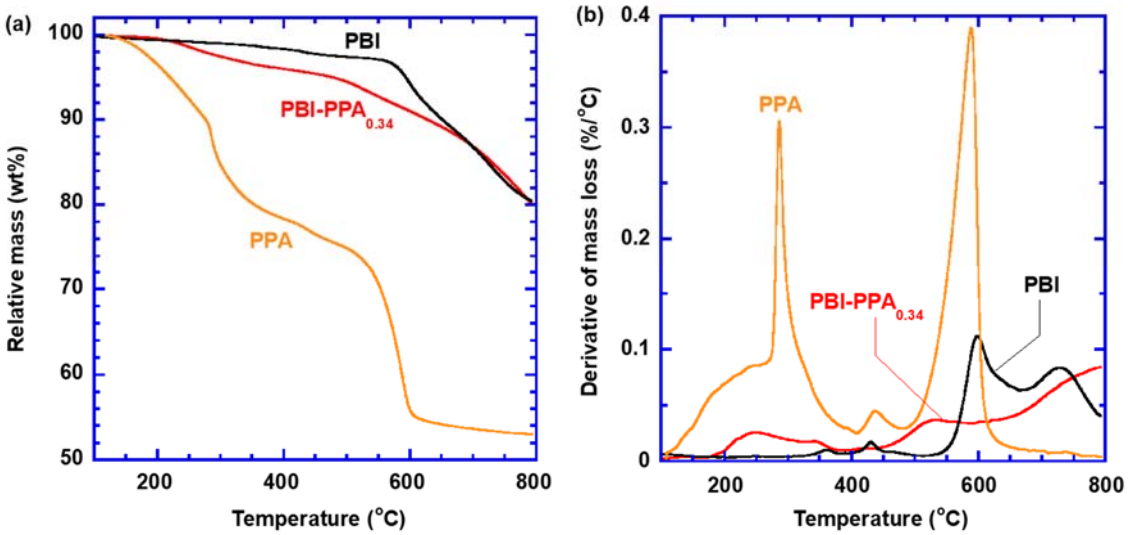

Fig. S4.

Thermal properties of PBI, PPA, and PBI-PPA$_{0.34}$. (a) Thermal gravimetric analysis (TGA) and (b) derivative thermogravimetric analysis (DTA) of PBI, PPA, and a representative PPA doped PBI sample, PBI-PPA$_{0.34}$.

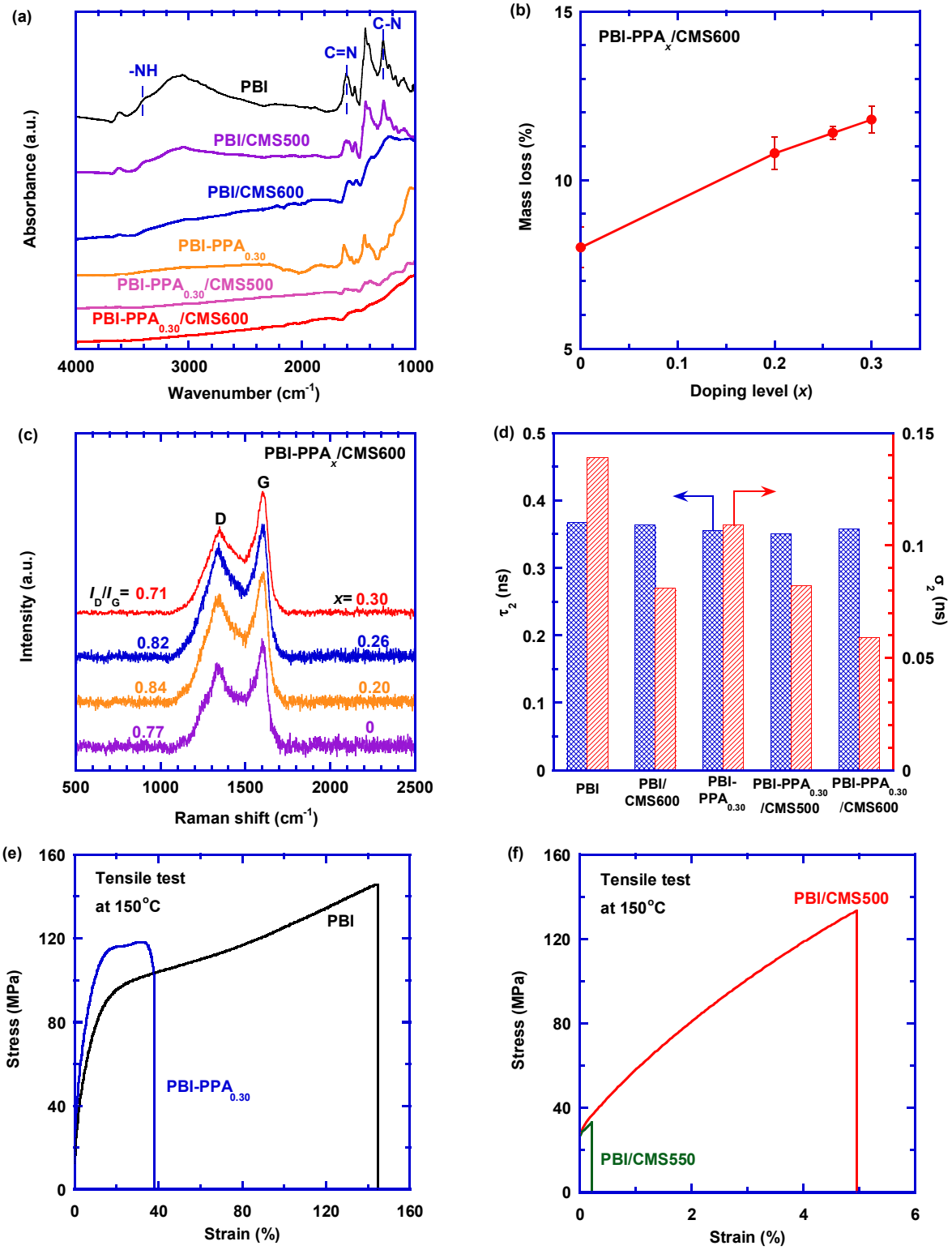
(a)
Absorbance (a.u.)
Wavenumber (cm-1)
-NH
C=N
C-N
PBI
PBI/CMS500
PBI/CMS600
PBI-PPA0.30
PBI-PPA0.30/CMS500
PBI-PPA0.30/CMS600
(b)
PBI-PPAx/CMS600
Mass loss (%)
Doping level (x)
(c)
PBI-PPAx/CMS600
Intensity (a.u.)
Raman shift (cm-1)
G
D
ID/IG= 0.71
0.82
0.84
0.77
x= 0.30
0.26
0.20
0
(d)
τ2 (ns)
σ2 (ns)
PBI
PBI/ CMS600
PBI- PPA0.30
PBI-PPA0.30 /CMS500
PBI-PPA0.30 /CMS600
(e)
Tensile test
at 150°C
Stress (MPa)
Strain (%)
PBI
PBI-PPA0.30
(f)
Tensile test
at 150°C
PBI/CMS500
PBI/CMS550
Stress (MPa)
Strain (%)

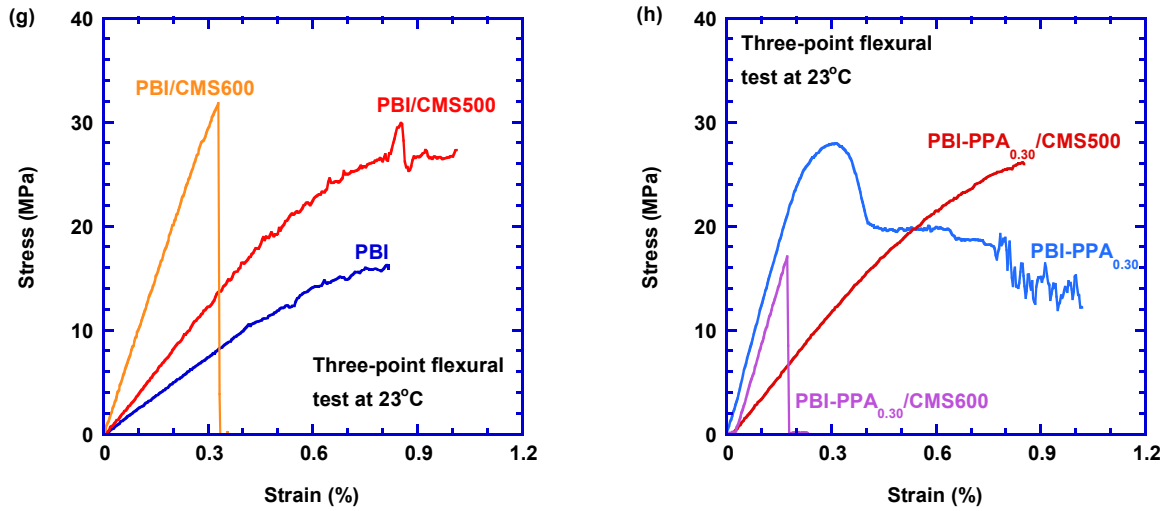

Fig. S5.

Physical properties of PBI-PPA/CMS films. (a) FTIR spectra of PBI, PBI/CMS600, PBI-PPA$_{0.30}$, PBI-PPA$_{0.30}$/CMS600. (b) Effect of the doping level on the mass loss of PBI-PPA when pyrolyzed at 600 °C. (c) Raman spectra of PBI-PPA/CMS600. (d) Average positron-electron annihilation lifetime (τ_2) and its corresponding distribution (σ_2). Strain-Stress tensile plots of (e) PBI and PBI-PPA$_{0.30}$ films, and (f) PBI/CMS500 and PBI/CMS550 films obtained using the tensile test at 150 °C. Strain-Stress tensile plots of (g) PBI and derived CMS films, and (h) PBI-PPA$_{0.30}$ and derived CMS films obtained using the three-point flexural test at 23 °C.

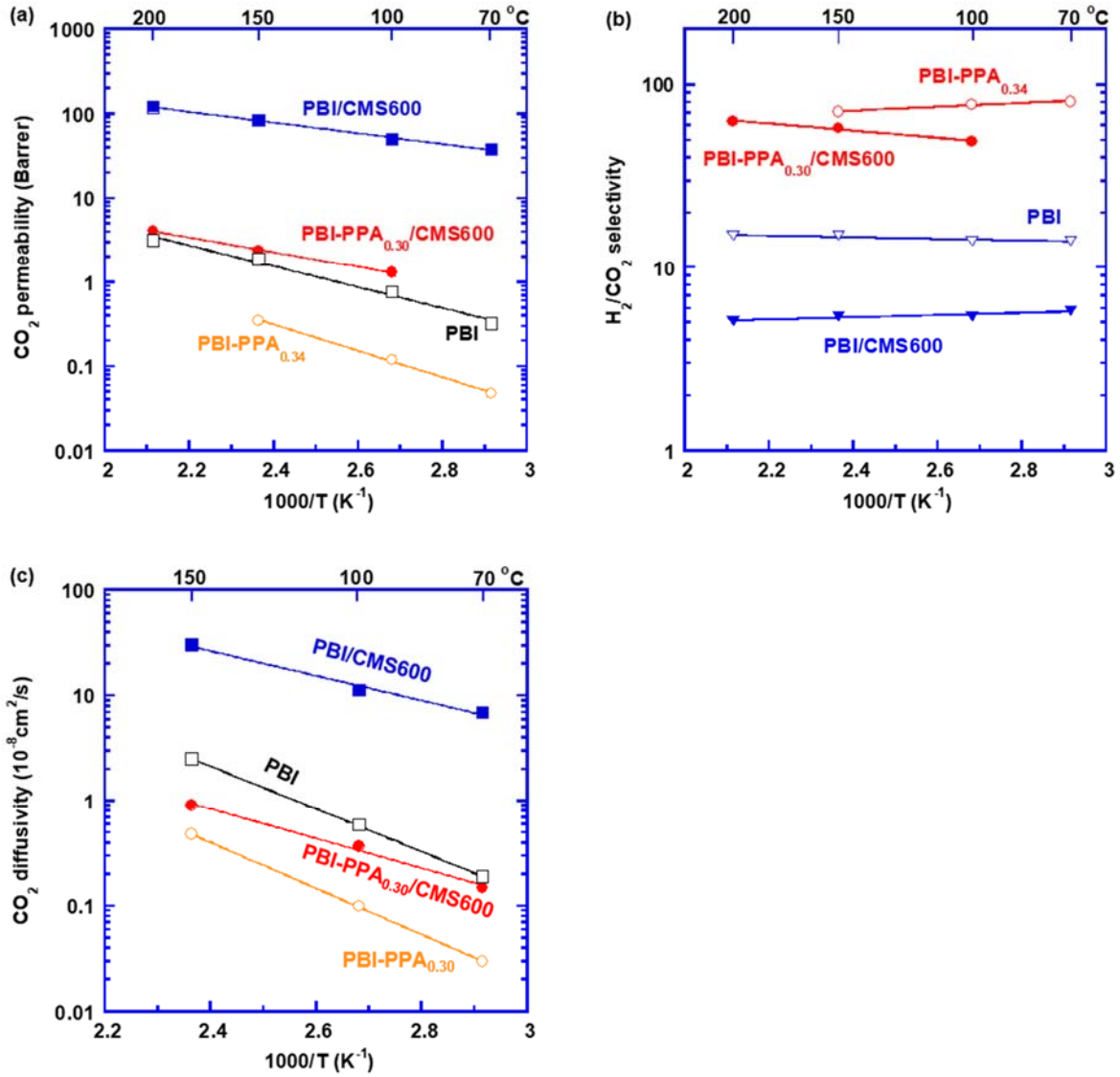

Fig. S6.

Effect of the temperature on pure-gas transport properties of the pristine and carbonized polymers. (a) CO_2 permeability, (b) H_2/CO_2 selectivity, and (c) CO_2 diffusivity of PBI, PBI-PPA$_{0.34}$, PBI/CMS600, and PBI-PPA$_{0.30}$/CMS600.

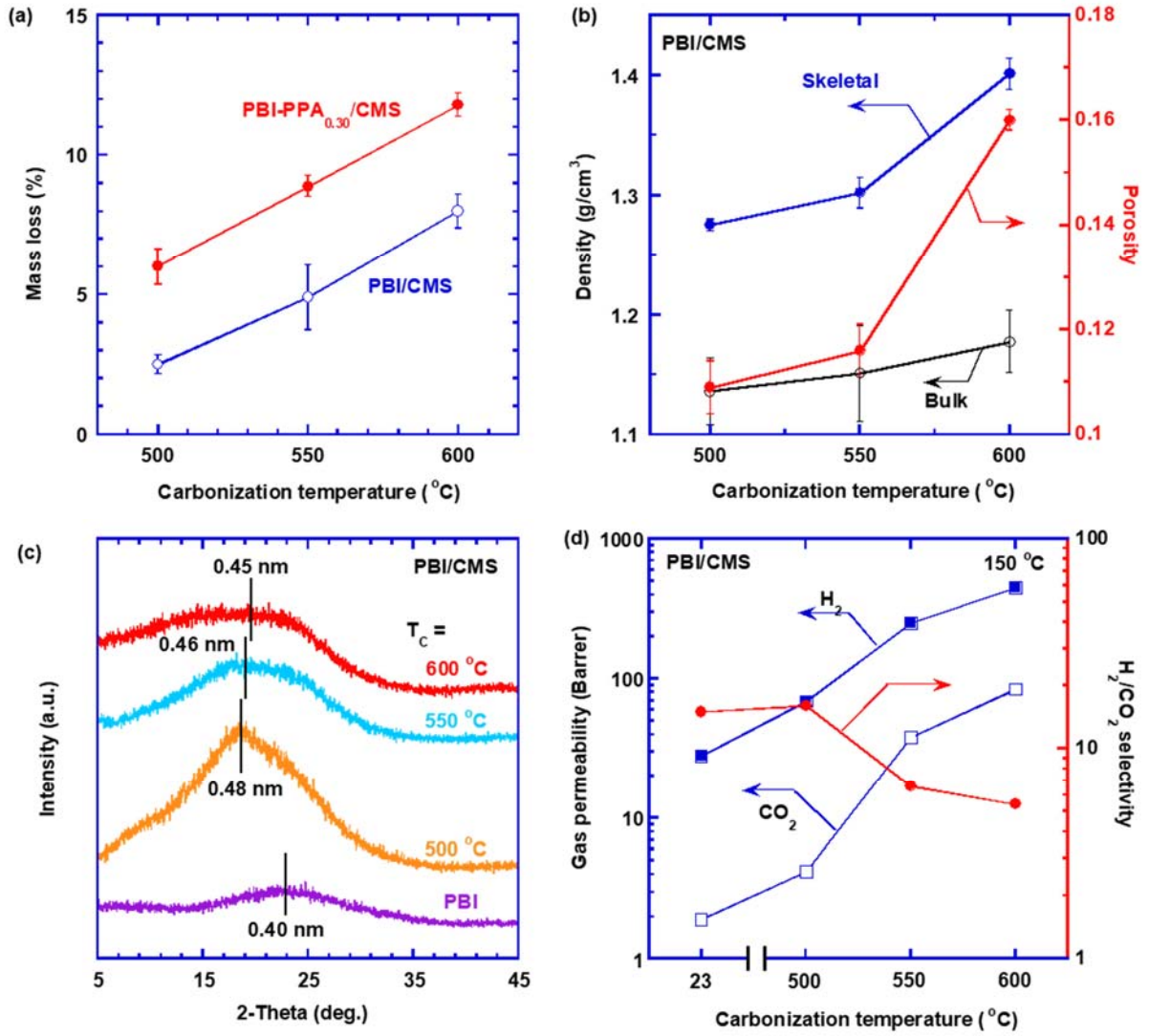

Fig. S7.
Effect of T_C on physical and gas transport properties of PBI/CMS and PBI-PPA$_{0.30}$/CMS. (a) Mass loss of PBI and PBI-PPA$_{0.30}$, (b) skeletal density, bulk density, and porosity, and (c) WAXD patterns of PBI/CMS samples. (d) Pure-gas H_2 and CO_2 permeability, and H_2/CO_2 selectivity of PBI/CMS at 150 °C.

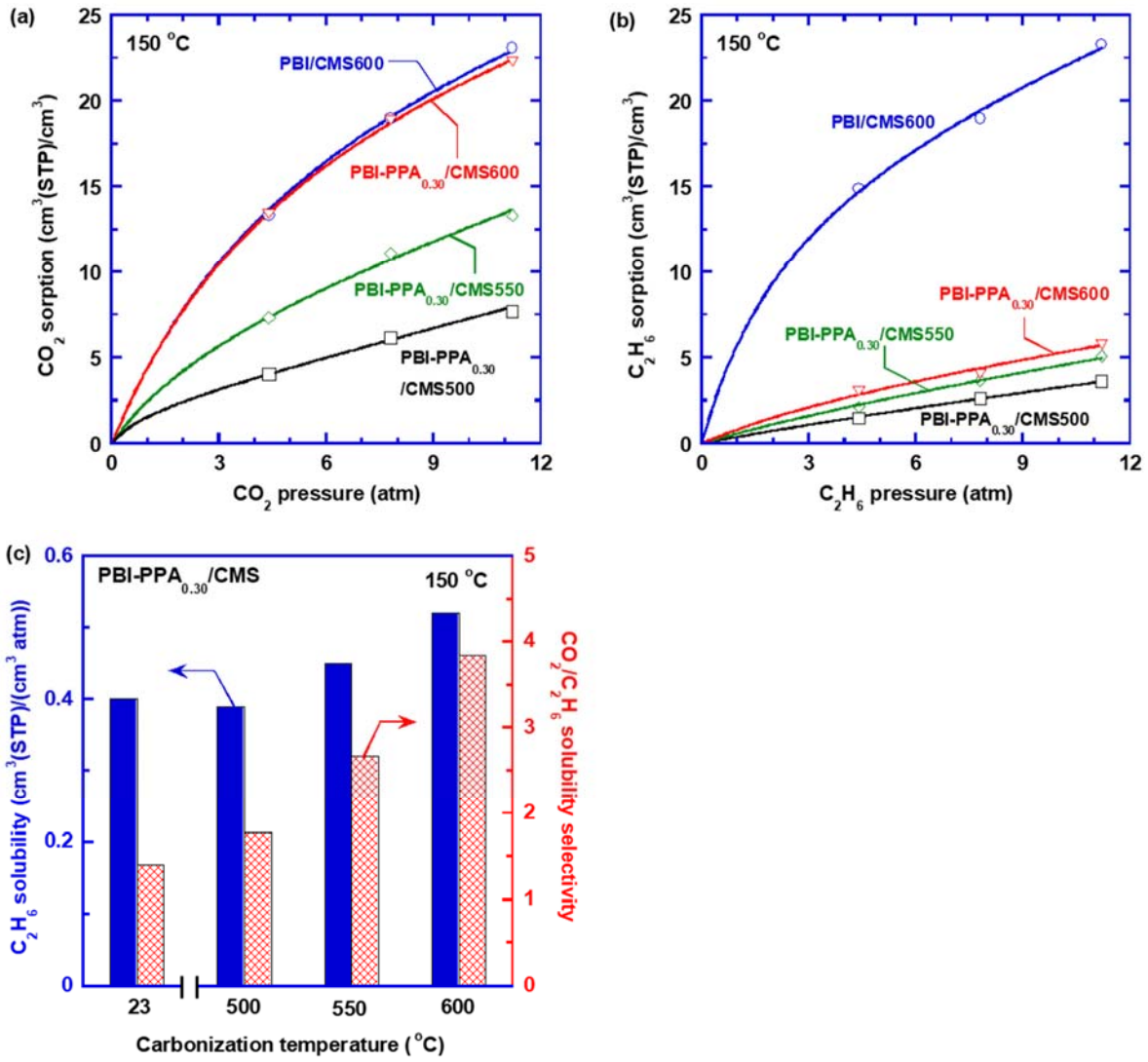

Fig. S8.

Gas sorption and solubility in PBI/CMS and PBI-PPA$_{0.30}$/CMS. (a) CO_2 and (b) C_2H_6 sorption isotherms of PBI/CMS600, PBI-PPA$_{0.30}$/CMS500, PBI-PPA$_{0.30}$/CMS550, and PBI-PPA$_{0.30}$/CMS600 at 150 °C. The curves are fittings using the dual-mode sorption model with the parameters shown in Table S5. (c) C_2H_6 solubility and CO_2/C_2H_6 solubility selectivity of PBI-PPA$_{0.30}$/CMS at 150 °C and 11 atm.

Table S1.

H_2/CO_2 separation properties in selected membrane materials for comparison (cf. Fig. 1F). Mixed-gas contains 50% CO_2 and 50% H_2.

	Materials		Mixed- or pure- gas	Temp. (°C)	H_2 perm. (Barrer)	H_2/CO_2 selectivity	Ref.
CMS in this study	1	PBI-$PPA_{0.34}$	Pure	150	25	71	This study
	2	PBI-$PPA_{0.30}$/CMS600	Pure	150	140	58	
			Mixed	150	116	33	
State-of-the-art CMS	3	PBI/CMS800	Pure	100	640	17	(*4*)
	4	PBI/CMS900	Pure	100	54	80	
		PBI/CMS900	Mixed	100	39	53	
	5	Kapton/CMS1000	Pure	50	7.2	161	(*40*)
	6	Kapton/CMS1100	Pure	50	0.32	343	
	7	P84/CMS900	Mixed	100	20	16	(*39*)
	8	PBI/Matrimid/CMS1000	Pure	35	91	25	(*38*)
	9	Cellophane/CMS600	Pure	30	39	59	(*44*)
	10	Cellulose/CMS700	Mixed	90	225	31	(*2*)
State-of-the-art polymers		PBI	Mixed	200	45	15	(*24*)
	11	PBI-TCL(6 h)	Pure	150	21	23	(*21*)
	12	PBI-$(H_3PO_4)_{0.16}$	Pure	150	12	35	(*24*)
		PBI-$(H_3PO_4)_{0.16}$	Mixed	150	12	34	
	13	PBI-$(H_3PO_4)_{1.0}$	Pure	150	1.5	140	
	14	PBI-$(H_2SO_4)_{0.24}$	Pure	150	7.4	47	
	15	PBI-$TBB_{0.213}$	Pure	150	9.6	24	(*25*)

Table S2.

H_2/CO_2 separation properties in selected inorganic membrane materials for comparison (cf. Fig. S1). Mixed-gas contains 50% CO_2 and 50% H_2.

Materials	Mixed- or pure- gas	Temp. (°C)	H_2 perm. (Barrer)	H_2/CO_2 selectivity	Ref.
Si600	Mixed	200	1493	71	(*45*)
Zeolite composite	Mixed	200	209	20	(*54*)
RUB-15	Mixed	200	67	106	(*16*)
2D $Zn_2(Bim)_4$	Mixed	200	5000	90	(*55*)
2D $Zn_2(Bim)_3$	Mixed	120	2400	166	(*56*)
GO	Pure	135	40	40	(*57*)
GO	Mixed	100	450	250	(*46*)
ZIF/GO	Mixed	250	388	14.9	(*58*)
iCONs	Mixed	150	2566	22.6	(*59*)
MXene	Mixed	25	32	27	(*60*)
MoS_2	Pure	160	1700	8	(*61*)
g-C_3N_4	Pure	250	1450	10	(*14*)
Calcined silica	Pure	200	60	36.4	(*62*)

Table S3.

Calculation of the *FFV* values for PBI-PPA films using the group contribution method at 23°C and 150°C.

Doping level (x)	PPA content (wt.%)	Vw (cm^3/mol)	ρ_b (g/cm^3)	23°C		$\bar{\alpha}_V$ (10^{-5} K^{-1})	150°C	
				V (cm^3/mol)	*FFV*		V (cm^3/mol)	*FFV*
0	0	154.6	1.286	239.5	0.161	6.9	241.6	0.168
0.23	11.7	170.6	1.357	257.1	0.137	9.8	260.4	0.148
0.34	16.4	178.3	1.384	266.3	0.130	11.1	270.0	0.142
0.42	19.5	183.9	1.401	273.2	0.125	11.9	277.4	0.138

Table S4.

Average positron-electron annihilation lifetime (τ_2) and its corresponding distribution (σ_2), o-Ps lifetimes and intensities of various samples. The standard deviations for all samples are based on the nonlinear least-squares fitting process carried out using a commercial software, where a reduced χ^2 of less than 1.1 was used as a metric to guide the assessment of model fit.

Samples	τ_{2av} (ns)	σ_2 (ns)	τ_3 (ns)	I_3 (%)
PBI	0.376 ± 0.003	0.109 ± 0.008	1.843 ± 0.023	18.1 ± 0.4
PBI/CMS600	0.364 ± 0.001	0.081 ± 0.003	--	--
PBI-$PPA_{0.30}$	0.361 ± 0.002	0.093 ± 0.007	1.733 ± 0.030	11.0 ± 0.3
PBI-$PPA_{0.30}$/CMS500	0.352 ± 0.002	0.076 ± 0.006	1.623 ± 0.056	4.1 ± 0.3
PBI-$PPA_{0.30}$/CMS600	0.358 ± 0.001	0.059 ± 0.003	--	--

Table S5.

Parameters of the dual-mode sorption model for CO_2 and C_2H_6 sorption in various samples at 150 °C.

Samples	CO_2			C_2H_6		
	k_D	b	C'_H	k_D	b	C'_H
PBI	0.23	0.12	6.7	0.36	0.24	5.9
PBI/CMS600	0.44	0.17	28	0.74	0.38	18
PBI-$PPA_{0.34}$	0.16	0.20	6.5	0.18	0.12	4.3
PBI-$PPA_{0.30}$/CMS500	0.42	0.37	3.7	0.25	0.078	1.7
PBI-$PPA_{0.30}$/CMS550	0.60	0.30	8.7	0.32	0.12	2.4
PBI-$PPA_{0.30}$/CMS600	0.41	0.17	27	0.31	0.16	3.5

Note: the units for k_D, b, and C'_H are $cm^3(STP)\ cm^{-3}\cdot atm^{-1}$, atm^{-1}, and $cm^3(STP)\ cm^{-3}$, respectively.

Table S6.

EDS analysis of the elemental composition of the cross-sections of a PBI-PPA$_{0.30}$ thick film and PBI-PPA$_{0.30}$/CMS600 film. Surface-center indicates the position between the surface and center.

Samples	Position	N/C molar ratio	P/C molar ratio
PBI thin film	Whole	0.36 ± 0.02	0
PBI-PPA$_{0.34}$ thin film	Whole	0.37± 0.02	0.034± 0.002
PBI-PPA$_{0.30}$ thick film	Surface	0.35 ± 0.01	0.032 ± 0.003
	Surface-center	0.35 ± 0.04	0.029 ± 0.002
	Center	0.36 ± 0.02	0.021 ± 0.001
	Whole	0.36 ± 0.03	0.028 ± 0.001
PBI-PPA$_{0.30}$/ CMS600 film	Surface	0.28 ± 0.02	0.030 ± 0.001
	Surface-center	0.27 ± 0.01	0.022 ± 0.003
	Center	0.28 ± 0.02	0.021 ± 0.002
	Whole	0.29 ± 0.02	0.027 ± 0.002

Table S7.

Young's modulus, tensile strength, and fracture strain of PBI, PBI-PPA$_{0.30}$, and their derived CMS films.

Samples	Young's modulus (MPa)[a]	Tensile Strength (MPa)[a]	Fracture Strain (%)[a]	Young's modulus (MPa)[b]	Fracture Strain (%)[b]
PBI	1435	145.9	144.4	2510	--
PBI/CMS500	2871	133.7	5.0	4060	--
PBI/CMS550	2911	33.1	0.2	--	--
PBI/CMS600	--	--	--	10,000	0.33
PBI-PPA$_{0.30}$	1984	118.3	37.7	12,300	--
PBI-PPA$_{0.30}$/CMS500	--	--	--	3940	--
PBI-PPA$_{0.30}$/CMS600	--	--	--	11,700	0.18

Note: [a] Data obtained using the tensile test at 150 °C. [b]Data obtained using the three-point flexural test at 23 °C.

Table S8

Summary of mechanical properties and H_2/CO_2 separation performance of reported PBI-based membranes and CMS membranes for H_2/CO_2 separation.

Samples	Young's modulus (GPa)	Tensile strength (MPa)	Fracture strain (%)	Temp. (℃)	H_2 permeability (Barrer)	H_2/CO_2 selectivity	Ref.
TADPS-TPA PBI	3.5	--	--	35	5.5	20	*(50)*
TADPS-IPA PBI	2.6	--	--	35	3.6	32	
TADPS-OBA PBI	2.1	--	--	35	5.7	10	
Undoped PANI/PBI (20/80)	1.81	26.06	0.29	30	3.79	3.6	*(51)*
Doped PANI/PBI (20/80)	2.06	30.19	12.83	30	0.841	2.6	
Celazole PBI	3.8	94	--	35	2.1	28	*(20)*
20/80 PI/PBI+1-IM TR400	4.0	109	3.0	35	3.1	42	
33/67 PI/PBI+1-IM TR400	3.9	110	3.0	35	5.3	29	
Cellulose/CMS550	2.07	--	--	130	1400	11.1	*(2)*
Cellulose/CMS700	5.69	--	--	130	773	49.5	
Cellulose/CMS850	7.53	--	--	130	445	83.9	

Table S9.

$E_{P,A}$ values for H_2 and CO_2 permeation in PBI, PBI-$PPA_{0.34}$, PBI/CMS600, and PBI-$PPA_{0.30}$/CMS600.

Samples	$E_{P,A}$ (kJ/mol)		$P_{A,0}$ ($\times 10^3$ Barrer)	
	H_2	CO_2	H_2	CO_2
PBI	24 ± 1	24 ± 1	25	1.5
PBI-$PPA_{0.34}$	28 ± 2	30 ± 2	71	1.7
PBI/CMS600	11 ± 1	12 ± 1	9.9	2.6
PBI-$PPA_{0.30}$/CMS600	21 ± 2	17 ± 2	52	0.29
PBI-$PPA_{0.30}$/CMS600 (mixed-gas)	21 ± 1	32 ± 1	42	31

Table S10.

$E_{P,A}$ values for CO_2 diffusion in PBI, PBI-$PPA_{0.34}$, PBI/CMS600, and PBI-$PPA_{0.30}$/CMS600.

Samples	$E_{D,A}$ (kJ/mol)	$D_{A,0}$ ($\times 10^{-5}$ cm^2/s)
PBI	39 ± 4	170
PBI-$PPA_{0.34}$	42 ± 5	70
PBI/CMS600	22 ± 2	17
PBI-$PPA_{0.30}$/CMS600	27 ± 3	2.0

REFERENCES AND NOTES

1. D. Y. Koh, B. A. McCool, H. W. Deckman, R. P. Lively, Reverse osmosis molecular differentiation of organic liquids using carbon molecular sieve membranes. *Science* **353**, 804–807 (2016).

2. L. Lei, F. Pan, A. Lindbråthen, X. Zhang, M. Hillestad, Y. Nie, L. Bai, X. He, M. D. Guiver, Carbon hollow fiber membranes for a molecular sieve with precise-cutoff ultramicropores for superior hydrogen separation. *Nat. Commun.* **12**, 268 (2021).

3. O. Sanyal, S. S. Hays, N. E. León, Y. A. Guta, A. K. Itta, R. P. Lively, W. J. Koros, A self-consistent model for sorption and transport in polyimide-derived carbon molecular sieve gas separation membranes. *Angew. Chem. Int. Ed.* **59**, 20343–20347 (2020).

4. M. Omidvar, H. Nguyen, Liang Huang, C. M. Doherty, A. J. Hill, C. M. Stafford, X. Feng, M. T. Swihart, H. Lin, Unexpectedly strong size-sieving ability in carbonized polybenzimidazole for membrane H_2/CO_2 separation. *ACS Appl. Mater. Interfaces* **11**, 47365–47372 (2019).

5. Y. Ma, M. L. Jue, F. Zhang, R. Mathias, H. Y. Jang, R. P. Lively, Creation of well-defined “mid-sized” micropores in carbon molecular sieve membranes. *Angew. Int. Ed. Chem.* **131**, 13393–13399 (2019).

6. J. Zhao, G. He, S. Huang, L. F. Villalobos, M. Dakhchoune, H. Bassas, K. V. Agrawal, Etching gas-sieving nanopores in single-layer graphene with an angstrom precision for high-performance gas mixture separation. *Sci. Adv.* **5**, eaav1851 (2019).

7. M. Shan, X. Liu, X. Wang, I. Yarulina, B. Seoane, F. Kapteijn, J. Gascon, Facile manufacture of porous organic framework membranes for precombustion CO_2 capture. *Sci. Adv.* **4**, eaau1698 (2018).

8. W. J. Koros, C. Zhang, Materials for next-generation molecularly selective synthetic membranes. *Nat. Mater.* **16**, 289–297 (2017).

9. H. Park, C. H. Jung, Y. M. Lee, A. J. Hill, S. J. Pas, S. T. Mudie, E. Van Wagner, B. D. Freeman, D. J. Cookson, Polymers with cavities tuned for fast selective transport of small molecules and ions. *Science* **318**, 254–258 (2007).

10. O. Sanyal, C. Zhang, G. B. Wenz, S. Fu, N. Bhuwania, L. Xu, M. Rungta, W. J. Koros, Next generation membranes -using tailored carbon. *Carbon* **127**, 688–698 (2018).

11. S. Kim, Y. M. Lee, Rigid and microporous polymers for gas separation membranes. *Prog. Polym. Sci.* **43**, 1–32 (2015).

12. M. Kiyono, P. J. Williams, W. J. Koros, Effect of pyrolysis atmosphere on separation performance of carbon molecular sieve membranes. *J. Membr. Sci.* **359**, 2–10 (2010).

13. L. X. Zhu, L. Huang, S. R. Venna, A. K. Blevins, Y. Ding, D. P. Hopkinson, M. T. Swihart, H. Lin, Scalable polymeric few-nanometer organosilica membranes with hydrothermal stability for selective hydrogen. *ACS Nano* **15**, 12119–12128 (2021).

14. L. F. Villalobos, M. T. Vahdat, M. Dakhchoune, Z. Nadizadeh, M. Mensi, E. Oveisi, D. Campi, N. Marzari, K. V. Agrawal, Large-scale synthesis of crystalline g-C_3N_4 nanosheets and high-temperature H_2 sieving from assembled films. *Sci. Adv.* **6**, eaay9851 (2020).

15. L. Zhu, D. Yin, Y. Qin, S. Konda, S. Zhang, A. Zhu, S. Liu, T. Xu, M. T. Swihart, H. Lin, Sorption-enhanced mixed matrix membranes with facilitated hydrogen transport for hydrogen purification and CO_2 capture. *Adv. Funct. Mater.* **29**, 1904357 (2019).

16. M. Dakhchoune, L. F. Villalobos, R. Semino, L. Liu, M. Rezaei, P. Schouwink, C. E. Avalos, P. Baade, V. Wood, Y. Han, M. Ceriotti, K. V. Agrawal, Gas-sieving zeolitic membranes fabricated by condensation of precursor nanosheets. *Nat. Mater.* **20**, 362–369 (2021).

17. H. Park, J. Kamcev, L. M. Robeson, M. Elimelech, B. D. Freeman, Maximizing the right stuff: The trade-off between membrane permeability and selectivity. *Science* **356**, eaab0530 (2017).

18. M. Galizia, W. S. Chi, Z. P. Smith, T. C. Merkel, R. W. Baker, B. D. Freeman, 50th Anniversary perspective: Polymers and mixed matrix membranes for gas and vapor separation: A review and prospective opportunities. *Macromolecules* **50**, 7809–7843 (2017).

19. L. Hu, S. Pal, H. Nguyen, V. Bui, H. Lin, Molecularly engineering polymeric membranes for H_2/CO_2 separation at 100–300 °C. *J. Polym. Sci.* **58**, 2467–2481 (2020).

20. J. D. Moon, A. T. Bridge, C. D'Ambra, B. D. Freeman, D. R. Paul, Gas separation properties of polybenzimidazole/thermally-rearranged polymer blends. *J. Membr. Sci.* **582**, 182–193 (2019).

21. L. Zhu, M. Swihart, H. Lin, Tightening polybenzimidazole (PBI) nanostructure via chemical cross-linking for membrane H_2/CO_2 separation. *J. Mater. Chem. A* **5**, 19914–19923 (2017).

22. X. Li, R. P. Singh, K. W. Dudeck, K. A. Berchtold, B. C. Benicewicz, Influence of polybenzimidazole main chain structure on H_2/CO_2 separation at elevated temperatures. *J. Membr. Sci.* **461**, 59–68 (2014).

23. L. Hu, V. T. Bui, L. Huang, R. P. Singh, H. Lin, Facilely cross-linking polybenzimidazole with polycarboxylic acids to improve H_2/CO_2 separation performance. *ACS Appl. Mater. Interfaces* **13**, 12521–12530 (2021).

24. L. Zhu, M. Swihart, H. Lin, Unprecedented size-sieving ability in polybenzimidazole doped with polyprotic acids for membrane H_2/CO_2 separation. *Energ. Environ. Sci.* **11**, 94–100 (2018).

25. A. Naderi, A. A. Tashvigh, T. S. Chung, H_2/CO_2 separation enhancement via chemical modification of polybenzimidazole nanostructure. *J. Membr. Sci.* **572**, 343–349 (2019).

26. H. Lin, M. Yavari, Upper bound of polymeric membranes for mixed-gas CO_2/CH_4 separations. *J. Membr. Sci.* **475**, 101–109 (2015).

27. Y. Cao, K. Zhang, O. Sanyal, W. J. Koros, Carbon molecular sieve membrane preparation by economical coating and pyrolysis of porous polymer hollow fibers. *Angew. Chem. Int. Ed.* **58**, 12149–12153 (2019).

28. W. Jiao, Y. Ban, Z. Shi, X. Jiang, Y. Li, W. Yang, Gas separation performance of supported carbon molecular sieve membranes based on soluble polybenzimidazole. *J. Membr. Sci.* **533**, 1–10 (2017).

29. Y. Xiao, T. S. Chung, Grafting thermally labile molecules on cross-linkable polyimide to design membrane materials for natural gas purification and CO_2 capture. *Energ. Environ. Sci.* **4**, 201–208 (2011).

30. C.-P. Hu, C. K. Polintan, L. L. Tayo, S.-C. Chou, H.-A. Tsai, W.-S. Hung, C.-C. Hu, K.-R. Lee, J.-Y. Lai, The gas separation performance adjustment of carbon molecular sieve membrane depending on the chain rigidity and free volume characteristic of the polymeric precursor. *Carbon* **143**, 343–351 (2019).

31. C. Zhang, W. J. Koros, Ultraselective carbon molecular sieve membranes with tailored synergistic sorption selective properties. *Adv. Mater.* **29**, 170163 (2017).

32. H. B. Park, Y. M. Lee, Fabrication and characterization of nanoporous carbon/silica membranes. *Adv. Mater.* **17**, 477–483 (2005).

33. J. S. Adams, A. K. Itta, C. Zhang, G. B. Wenz, O. Sanyal, W. J. Koros, New insights into structural evolution in carbon molecular sieve membranes during pyrolysis. *Carbon* **141**, 238–246 (2019).

34. O. Salinas, X. Ma, Y. Wang, Y. Han, I. Pinnau, Carbon molecular sieve membrane from a microporous spirobisindane-based polyimide precursor with enhanced ethylene/ethane mixed-gas selectivity. *RSC Adv.* **7**, 3265–3272 (2017).

35. S. Fu, G. B. Wenz, E. S. Sanders, S. S. Kulkarni, W. Qiu, C. Ma, W. J. Koros, Effects of pyrolysis conditions on gas separation properties of 6FDA/DETDA: DABA (3: 2) derived carbon molecular sieve membranes. *J. Membr. Sci.* **520**, 699–711 (2016).

36. J. M. Pérez-Francisco, J. L. Santiago-García, M. I. Loría-Bastarrachea, D. R. Paul, B. D. Freeman, M. Aguilar-Vega, CMS membranes from PBI/PI blends: Temperature effect on gas transport and separation performance. *J. Membr. Sci.* **597**, 117703 (2020).

37. L. Xu, M. Rungta, W. J. Koros, Matrimid® derived carbon molecular sieve hollow fiber membranes for ethylene/ethane separation. *J. Membr. Sci.* **380**, 138–147 (2011).

38. S. S. Hosseini, T. S. Chung, Carbon membranes from blends of PBI and polyimides for N_2/CH_4 and CO_2/CH_4 separation and hydrogen purification. *J. Membr. Sci.* **328**, 174–185 (2009).

39. E. P. Favvas, E. P. Kouvelos, G. E. Romanos, G. I. Pilatos, A. C. Mitropoulos, N. K. Kanellopoulos, Characterization of highly selective microporous carbon hollow fiber membranes prepared from a commercial co-polyimide precursor. *J. Porous Mater.* **15**, 625–633 (2008).

40. H. Hatori, H. Takagi, Y. Yamada, Gas separation properties of molecular sieving carbon membranes with nanopore channels. *Carbon* **42**, 1169–1173 (2004).

41. K. Hazazi, X. Ma, Y. Wang, W. Ogieglo, A. Alhazmi, Y. Han, I. Pinnau, Ultra-selective carbon molecular sieve membranes for natural gas separations based on a carbon-rich intrinsically microporous polyimide precursor. *J. Membr. Sci.* **585**, 1–9 (2019).

42. X. Ma, J. Lin, in *Modern Inorganic Synthetic Chemistry* (Elsevier, 2017), pp. 669–686.

43. N. Du, H. B. Park, G. P. Robertson, M. M. Dal-Cin, T. Visser, L. Scoles, M. D. Guiver, Polymer nanosieve membranes for CO_2-capture applications. *Nat. Mater.* **10**, 372–375 (2011).

44. M. C. Campo, F. D. Magalhaes, A. Mendes, Carbon molecular sieve membranes from cellophane paper. *J. Membr. Sci.* **350**, 180–188 (2010).

45. R. M. De Vos, H. Verweij, High-selectivity, high-flux silica membranes for gas separation. *Science* **279**, 1710–1711 (1998).

46. H. Li, Z. Song, X. Zhang, Y. Huang, S. Li, Y. Mao, H. J. Ploehn, Y. Bao, M. Yu, Ultrathin, molecular-sieving graphene oxide membranes for selective hydrogen separation. *Science* **342**, 95–98 (2013).

47. M. Myglovets, O. I. Poddubnaya, O. Sevastyanova, M. E. Lindström, B. Gawdzik, M. Sobiesiak, M. M. Tsyba, V. I. Sapsay, D. O. Klymchuk, A. M. Puziy, Preparation of carbon adsorbents from lignosulfonate by phosphoric acid activation for the adsorption of metal ions. *Carbon* **80**, 771–783 (2014).

48. L. Hu, J. Liu, L. Zhu, X. Hou, L. Huang, H. Lin, J. Cheng, Highly permeable mixed matrix materials comprising ZIF-8 nanoparticles in rubbery amorphous poly(ethylene oxide) for CO_2 capture. *Sep. Purif. Technol.* **205**, 58–65 (2018).

49. B. Schultrich, H. J. Scheibe, G. Grandremy, D. Schneider, Elastic modulus of amorphous carbon films. *Phys. Status Solidi* **145**, 385–392 (1994).

50. H. Borjigin, K. A. Stevens, R. Liu, J. D. Moon, A. T. Shaver, S. Swinnea, B. D. Freeman, J. S. Riffle, J. E. McGrath, Synthesis and characterization of polybenzimidazoles derived from tetraaminodiphenylsulfone for high temperature gas separation membranes. *Polymer* **71**, 135–142 (2015).

51. V. Giel, J. Kredatusová, M. Trchová, J. Brus, J. Žitka, J. Peter, Polyaniline/polybenzimidazole blends: Characterisation of its physico-chemical properties and gas separation behaviour. *Eur. Polym. J.* **77**, 98–113 (2016).

52. S. Gadipelli, W. Travis, W. Zhou, Z. Guo, A thermally derived and optimized structure from ZIF-8 with giant enhancement in CO_2 uptake. *Energ. Environ. Sci.* **7**, 2232–2238 (2014).

53. T. Sugama, Hydrothermal degradation of polybenzimidazole coating. *Mater. Lett.* **58**, 1307–1312 (2004).

54. M. Yu, H. H. Funke, R. D. Noble, J. L. Falconer, H_2 separation using defect-free, inorganic composite membranes. *J. Am. Chem. Soc.* **133**, 1748–1750 (2011).

55. Y. Peng, Y. Li, Y. Ban, H. Jin, W. Jiao, X. Liu, W. Yang, Metal-organic framework nanosheets as building blocks for molecular sieving membranes. *Science* **346**, 1356–1359 (2014).

56. Y. Peng, Y. Li, Y. Ban, W. Yang, Two-dimensional metal-organic framework nanosheets for membrane-based gas separation. *Angew. Chem. Int. Ed.* **56**, 9757–9761 (2017).

57. H. W. Kim, H. W. Yoon, S.-M. Yoon, B. M. Yoo, B. K. Ahn, Y. H. Cho, H. J. Shin, H. Yang, U. Paik, S. Kwon, J.-Y. Choi, H. B. Park, Selective gas transport through few-layered graphene and graphene oxide membranes. *Science* **342**, 91–95 (2013).

58. A. Huang, Q. Liu, N. Wang, Y. Zhu, J. Caro, Bicontinuous zeolitic imidazolate framework ZIF-8@GO membrane with enhanced hydrogen selectivity. *J. Am. Chem. Soc.* **136**, 14686–14689 (2014).

59. Y. Ying, M. Tong, S. Ning, S. K. Ravi, S. B. Peh, S. C. Tan, S. J. Pennycook, D. Zhao, Ultrathin two-dimensional membranes assembled by ionic covalent organic nanosheets with reduced apertures for gas separation. *J. Am. Chem. Soc.* **142**, 4472–4480 (2020).

60. J. Shen, G. Liu, Y. Ji, Q. Liu, L. Cheng, K. Guan, M. Zhang, G. Liu, J. Xiong, J. Yang, W. Jin, 2D MXene nanofilms with tunable gas transport channels. *Adv. Funct. Mater.* **28**, 1801511 (2018).

61. A. Achari, S. Sahana, M. Eswaramoorthy, High performance MoS_2 membranes: Effects of thermally driven phase transition on CO_2 separation efficiency. *Energ. Environ. Sci.* **9**, 1224–1228 (2016).

62. H. Song, Y. Wei, H. Qi, Tailoring pore structures to improve the permselectivity of organosilica membranes by tuning calcination parameters. *J. Mater. Chem. A* **5**, 24657–24666 (2017).